CORA Cork Open Research Archive
Cartlann Taighde Oscailte Chorcaí

Title	A comprehensive K 2 and ground-based study of CRTS J035905.9+175034, an eclipsing SU UMa system with a large mass ratio
Authors	Littlefield, Colin;Garnavich, Peter M.;Kennedy, Mark R.;Szkody, Paula;Zhibin, Dai
Publication date	2018-05-14
Original Citation	Littlefield, C., Garnavich, P., Kennedy, M. and Szkody, P. (2018) 'A Comprehensive K 2 and Ground-based Study of CRTS J035905.9+175034, an Eclipsing SU UMa System with a Large Mass Ratio', The Astronomical Journal, 155(6), 232 (13 pp). doi: 10.3847/1538-3881/aabcd1
Type of publication	Article (peer-reviewed)
Link to publisher's version	http://stacks.iop.org/1538-3881/155/i=6/a=232 - 10.3847/1538-3881/aabcd1
Rights	© 2018. The American Astronomical Society. All rights reserved
Download date	2026-11-04 17:16:07
Item downloaded from	https://hdl.handle.net/10468/6642

UCC
University College Cork, Ireland
Coláiste na hOllscoile Corcaigh

The Astronomical Journal, 155:232 (13pp), 2018 June https://doi.org/10.3847/1538-3881/aabcd1
© 2018. The American Astronomical Society. All rights reserved.

A Comprehensive *K*2 and Ground-based Study of CRTS J035905.9+175034, an Eclipsing SU UMa System with a Large Mass Ratio

Colin Littlefield[1], Peter Garnavich[1], Mark Kennedy[2], Paula Szkody[3], and Zhibin Dai[4,5,6]
[1] Department of Physics, University of Notre Dame, Notre Dame, IN 46556, USA
[2] Department of Physics, University College Cork, Cork, Ireland
[3] Department of Astronomy, University of Washington, Seattle, WA 98195, USA
[4] Yunnan Observatories, Chinese Academy of Sciences, 396 Yangfangwang, Guandu District, Kunming, 650216, People's Republic of China
[5] Key Laboratory for the Structure and Evolution of Celestial Objects, Chinese Academy of Sciences, 396 Yangfangwang, Guandu District, Kunming, 650216, People's Republic of China
[6] Center for Astronomical Mega-Science, Chinese Academy of Sciences, 20A Datun Road, Chaoyang District, Beijing, 100012, People's Republic of China
Received 2017 September 27; revised 2018 April 5; accepted 2018 April 7; published 2018 May 14

Abstract

CRTS J035905.9+175034 is the first eclipsing SU UMa system for which a superoutburst has been observed by *Kepler* in the short-cadence mode. The light curve contains one superoutburst, eight normal outbursts (including a precursor to the superoutburst), and several minioutbursts that are present before—but not after—the superoutburst. The superoutburst began with a precursor normal outburst, and shortly after the peak of the precursor, the system developed large-amplitude superhumps that achieved their maximum amplitude after just three superhump cycles. The period excess of the initial superhump period relative to the orbital period implies a mass ratio of 0.281 ± 0.015, placing it marginally above most theoretical predictions of the highest-possible mass ratio for superhump formation. In addition, our analysis of the variations in eclipse width and depth, as well as the hot spot amplitudes, generally provides substantiation of the thermal-tidal instability model. The *K*2 data, in conjunction with our ground-based time-resolved spectroscopy and photometry from 2014 to 2016, allows us to determine many of the fundamental parameters of this system.

Key words: accretion, accretion disks – novae, cataclysmic variables – stars: individual (CRTS J035905.9 +175034)

1. Introduction

Dwarf novae consist of a low-mass donor star that overfills its Roche lobe and loses mass to a white dwarf primary (WD). An accretion disk forms around the WD and undergoes occasional photometric outbursts, usually with amplitudes of several magnitudes and lasting for several days. One subset of dwarf novae, the SU UMa systems, show two discrete types of outbursts: normal outbursts and superoutbursts. Superoutbursts are brighter than normal outbursts by about one magnitude and last significantly longer. The light curve of a superoutburst exhibits superhumps, which are periodic modulations whose period is several percent longer than the orbital period. The interval between consecutive superoutbursts is known as a supercycle.

Normal outbursts are postulated to occur as a result of a thermal disk instability (Osaki 1974). Mass transfer from the secondary causes the disk density to exceed a critical value, leading to the ionization of hydrogen and an ensuing thermal runaway as the disk becomes optically thick. The increased disk viscosity boosts the accretion rate onto the WD before a cooling front extinguishes the outburst. Despite the elevated accretion rate, the disk still gains mass during a normal outburst.

The thermal-tidal instability (TTI) model (Osaki 1989) is the prevailing theory regarding the mechanism of superoutbursts. According to the TTI model, superoutbursts occur when the outer radius of the disk expands to the 3:1 Lindblad resonance, at which point tidal interactions with the donor cause the disk to become eccentric and to undergo apsidal precession. The superhumps appear once the disk becomes eccentric, and the enhanced tidal dissipation of the disk's angular momentum causes increased accretion onto the WD. Critically, the TTI model makes a fundamental prediction that during any given supercycle, each normal outburst will force the outer disk radius to expand until the 3:1 resonance radius is reached.

During a superoutburst, the superhump period changes, and an O–C diagram of the superhump maxima will generally display three distinct regimes: Stages A, B, and C (Kato et al. 2009). Stage A superhumps are the first superhumps to appear in a superoutburst, and they have the longest period. Kato & Osaki (2013) argued that they are observed when the disk eccentricity is confined to the 3:1 resonance and that their period is equivalent to the dynamical precession rate at that resonance. At the end of Stage A, the superhump period decreases abruptly, marking the transition to Stage B. Whereas the superhump period during Stage A is constant, Stage B superhumps usually show a positive period derivative, related to a pressure effect within the disk (Kato & Osaki 2013). Finally, Stage C superhumps appear after Stage B, have a shorter period than Stage B, and do not show a period derivative.

The continuous photometry made possible by the *Kepler* satellite has provided significant insight into the behavior of SU UMa systems, enabling a test of the TTI model's predictions. For example, Osaki & Kato (2014) found that each superoutburst in *Kepler* data of V1504 Cyg began with a precursor normal outburst, with superhumps appearing at the maximum of the precursor. They also reported evidence that the system's disk radius increases during its supercycle. Both of these observations supported key predictions of the TTI model.

We report short-cadence *Kepler* observations and ground-based spectroscopy and photometry of the poorly studied cataclysmic variable CRTS J035905.9+175034 (= MLS130302:035906 +175034; hereinafter J0359). Our data reveal it to be an eclipsing SU UMa system with an orbital period of 1.91 hr. This object appears in the Sloan Digital Sky Survey Data Release 9 as SDSS J035905.91+175034.47 with $g = 18.50$ and colors $u - g = 0.91$ and $g - r = 0.46$, and it is listed as a newly discovered cataclysmic variable in Drake et al. (2014).

2. Data

2.1. K2 Observations

The *Kepler* spacecraft observed J0359 from 2015 February 2 to April 24, as part of Campaign 4 of the *K*2 mission (Howell et al. 2014). The data were taken in short-cadence mode, with a typical cadence of 58.8 s per image. The data set spans 70.9 days, providing nearly continuous coverage during that time. A light curve was constructed by using PYKE (Still & Barclay 2012) to extract events from the target pixel file. There were occasional, brief gaps in the light curve when onboard thrusters were fired to keep the spacecraft pointing at the campaign field, but these data were removed by deleting observations that had a QUALITY flag > 0.

2.2. Ground-based Spectroscopy

We obtained spectra of J0359 with the Large Binocular Telescope and the Multi-Object Dual Spectrograph (MODS) on two occasions. Observations were taken on 2015 October 14 (UT) using MODS1 (SX mirror) through a 1.2 arcsec wide slit in the grating mode, providing a resolution of 1300. Ten 200 s exposures were obtained with 90 s of overhead between spectra. The data spanned 40% of the orbital period, including an eclipse.

The LBT also obtained spectra on 2016 January 3 (UT) with the MODS1 spectrograph. A 1.0 arcsec slit was employed with the grating mode, providing a resolution of 1500. On this visit, 27 spectra were obtained, each with a 200 s exposure time. The CCD was binned by two in the spatial direction, reducing the overhead to 60 s, and the spectral sequence covers slightly more that one full orbit of the system. In both visits, the position angle of the slit was rotated to match the parallactic angle.

The spectra were bias-subtracted, flat-fielded, extracted using IRAF *twodspec* routines, and wavelength-calibrated using Ne and Ar emission arcs taken during the day. We used airglow lines extracted in the sky subtraction to refine the wavelength solution. Finally, the spectra were flux-calibrated from observations of the spectrophotometric standard G191-B2B.

Spectra were also obtained with the Apache Point Observatory 3.5 m telescope on three occasions during 2014–2015 using the Double Imaging Spectrograph with the high resolution gratings, giving a resolution of 0.6 Å from 4000 to 5000 Å in the blue and 6000–7200 Å in the red. Two spectra were also obtained with the Kitt Peak 4 m telescope and RC Spectrograph using the second order of grating KPC-22b, resulting in a wavelength coverage of 3800–4900 Å at a resolution of 0.7 Å. As with the LBT data, the spectra and calibration lamps and flux standards were reduced using IRAF routines. The observations are summarized in Table 1. Because the spectra were similar to the LBT but with reduced signal-to-noise ratio and time resolution, most of the analysis in this paper uses the LBT spectra.

Table 1
Summary of Observations

UT Date	Site	Observations
2005 Sep 25–2013 Dec 23	CSS+MLS	sporadic photometry
2014 Aug 23	KPNO 4 m	2 × 1050 s spectra
2014 Nov 21	APO 3.5 m	18 × 600 s spectra
2015 Feb 7–Apr 24	*K2*	SC continuous photometry
2015 Oct 14	LBT 8.4 m	10 × 200 s spectra
2015 Oct 17	APO 3.5 m	5 × 600 s spectra
2015 Dec 18	APO 3.5 m	2 × 600 s spectra
2015 Dec 27	China 1 m	207 × 25 s photometry
2016 Jan 3	LBT 8.4 m	27 × 200 s spectra + 204 × 15 s phot

2.3. Ground-based Photometry

We acquired photometry on 2015 December 27 using a 1 m Cassegrain telescope and an Andor DZ936 camera at Weihai Observatory at Shandong University in Weihei City, China (Hu et al. 2014). The exposure time was 25 s, and the observations lasted for 1.5 hr. One eclipse was observed, with the light curve showing no evidence of a pre-eclipse hump.

During the 2016 LBT run, the Large Binocular Camera (LBC) obtained photometry simultaneously with the spectra. The exposure time was 15.24 s through a Bessel *V* filter, and to improve the time resolution, only 1000 rows of the central chip were read out. In all, we took 204 images between 4:20 and 6:24 UT, with an average time between exposures of 35.6 s. We performed aperture photometry of J0359 and nearby stars, calibrating the data to the *V*-band using the APASS catalog. The typical brightness of J0359 outside of eclipse ranged between *V* magnitudes 17.9–18.2. The light curve included one eclipse and a low-amplitude pre-eclipse hump attributable to the stream-disk hot spot. After removing observations obtained during eclipse and detrending the light curve by subtracting a third-order polynomial, we identified a low-amplitude quasi-periodic oscillation with a period of 3.5 minutes of unknown origin (Figure 1).

The Catalina Real Time Transient Survey (CRTS; Drake et al. 2009) provides a much longer baseline of observations than our time-series photometry. CRTS observed J0359 from 2005 September 25 until 2013 December 23 using the Catalina 0.7 m Schmidt telescope and the Mt. Lemmon 1.5 m telescope. These data are shown in Figure 2. Many outbursts are evident in this data set, along with numerous points obtained during eclipses.

3. *K*2 Photometry Analysis

As shown in Figure 3, the *K*2 light curve contains one superoutburst and eight normal outbursts, one of which is a precursor to the superoutburst. Prior to the superoutburst, there were a number of minioutbursts that recurred quasi-periodically every ∼2 days with amplitudes of ∼0.5 mag. The minioutbursts had irregular morphologies and partially overlapped with each other to such an extent that it is almost impossible to identify the quiescent level between the first four normal outbursts. There are none after the superoutburst. We discuss these minioutbursts in Section 5.4.

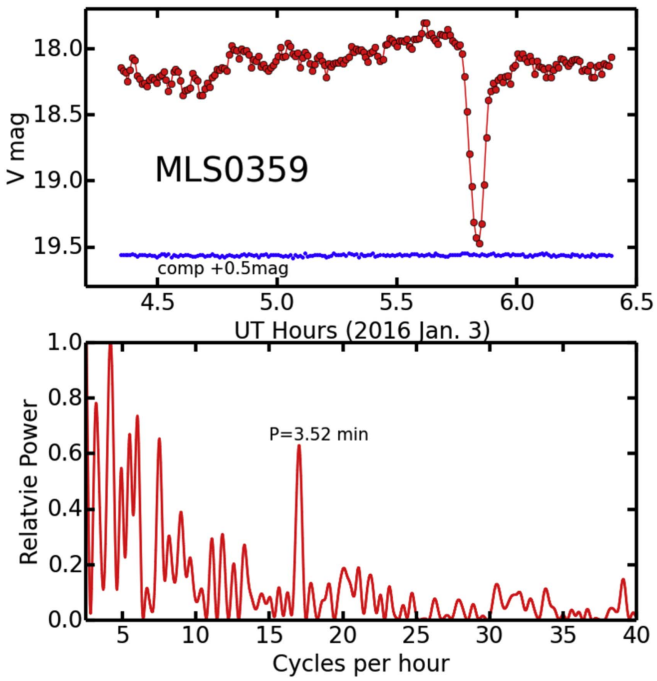


Figure 1. Top panel: the light curve of J0359 obtained with the LBT/LBC simultaneously with the MODS spectroscopy in 2016. The data has twice the cadence of the K2 photometry. Bottom panel: a periodogram of the LBC light curve, showing significant power at 3.5 minutes. The variation is not seen in the *K*2 data or the other photometry, suggesting that this is a quasi-periodic oscillation.

To extract the depth, width, and time of minimum light of the eclipses, we fitted polynomials to all eclipses, except for those with incomplete coverage. We visually inspected the fits to ensure their adequacy. The eclipse depth was defined as the ratio of the flux at minimum light to the median out-of-eclipse flux within one orbital cycle of the eclipse; this approach works well for quiescent data and normal outbursts, but it struggles to accurately measure depth when superhumps are present. The width was estimated by numerically determining the full width at half minimum (FWHM) for each polynomial. These parameters are included in the lower panels in Figure 3. Figure 4 enlarges the superoutburst light curve and the eclipse O–C and depth plots so that details may be seen more distinctly.

The times of mid-eclipse are well described by the orbital ephemeris of

$$T_{\rm min}[{\rm BJD}] = 2457069.9825(2) + 0.079555141(15) \times E,$$

where the numbers in parentheses give the 1σ uncertainties on the final digits of the corresponding parameters. We show the adequacy of this ephemeris by plotting the eclipse O–C residuals in Figure 3.

The trailed Lomb–Scargle periodogram in Figure 3 shows the evolution of the power spectrum near the orbital frequency throughout the *K*2 light curve. To generate it, we created a smoothed light curve using the LOWESS algorithm (Cleveland 1979) and subtracted it from the unsmoothed light curve. We excluded observations between $0.9 < \phi_{\rm orb} < 1.1$ to reduce the signal from eclipses. We then calculated the power spectrum with the brightness expressed in flux (not magnitudes) using a window width of 1.5 days and a step size of 0.15 days.

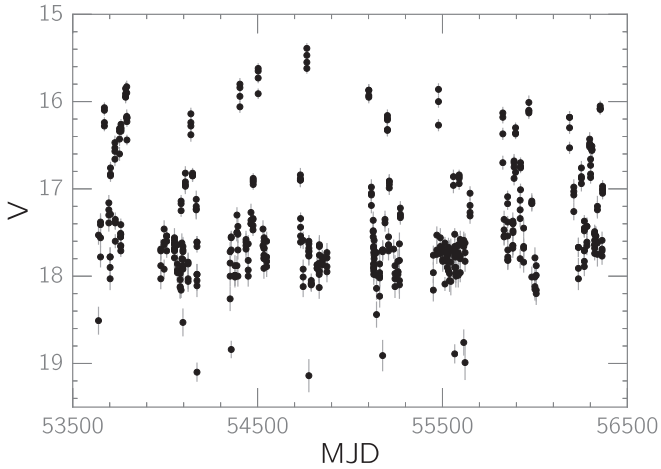


Figure 2. The CRTS light curve of J0359. Frequent outbursts are apparent, as are several eclipses.

Outside of the superoutburst, the power was concentrated at the orbital period and its harmonics. Near the peak of the second normal outburst, the power briefly shifted to a slightly lower frequency for about a half-day before returning to the orbital frequency. At the start of the superoutburst, the superhump frequency appeared, quickly increased in frequency, and stabilized, disappearing as the system returned to quiescence. Throughout the superoutburst, the interaction of eclipses and superhumps caused the power to oscillate between the orbital and superhump frequencies, a phenomenon that persisted until the very end of the superoutburst. Other than the orbital and superhump harmonics, the power spectrum did not show evidence of additional periodicities, such as the candidate quasi-periodic observation detected in one ground-based light curve (Figure 1).

The phased light curve of the quiescent orbital modulation (Figure 5), which showed a deep, 1.3 mag eclipse preceded by an orbital hump from the stream-disk collision, is typical of high-inclination CVs. However, individual orbital cycles showed highly variable morphologies. Dips occurred sporadically at nearly every orbital phase, and the amplitude of the orbital hump was highly variable, ranging from less than 0.1 to 0.3 mag. Moreover, the hot spot hump usually peaked before the eclipse, but in a minority of orbits, it appeared to peak at the time of eclipse and was equally visible before and after the eclipse.

We used the Eclipsing Light Curve (ELC) code from Orosz & Hauschildt (2000) to model part of the quiescent light curve in order to derive physical parameters of the system (Figure 5). We set the mass ratio to 0.28 (per Section 5.1), the effective secondary temperature to 3000 K (in line with the effective secondary temperature for the given orbital period predicted by Knigge et al. 2011), and X-ray luminosity of the WD to 10^{29} erg cm^{-2} s^{-1} (in line with the system being a dwarf nova, which typically have low X-ray luminosities). Based on the lack of WD absorption lines (Section 4), the spectrum suggests that the accretion disk is dominant at optical wavelengths. In keeping with this, we neglected optical light from the WD in our models by setting the effective temperature of the WD to a negative value. After setting the orbital separation to 0.73 $R_\odot$ and allowing the outer accretion disk radius, inner accretion disk temperature, orbital inclination, and hot-spot parameters to

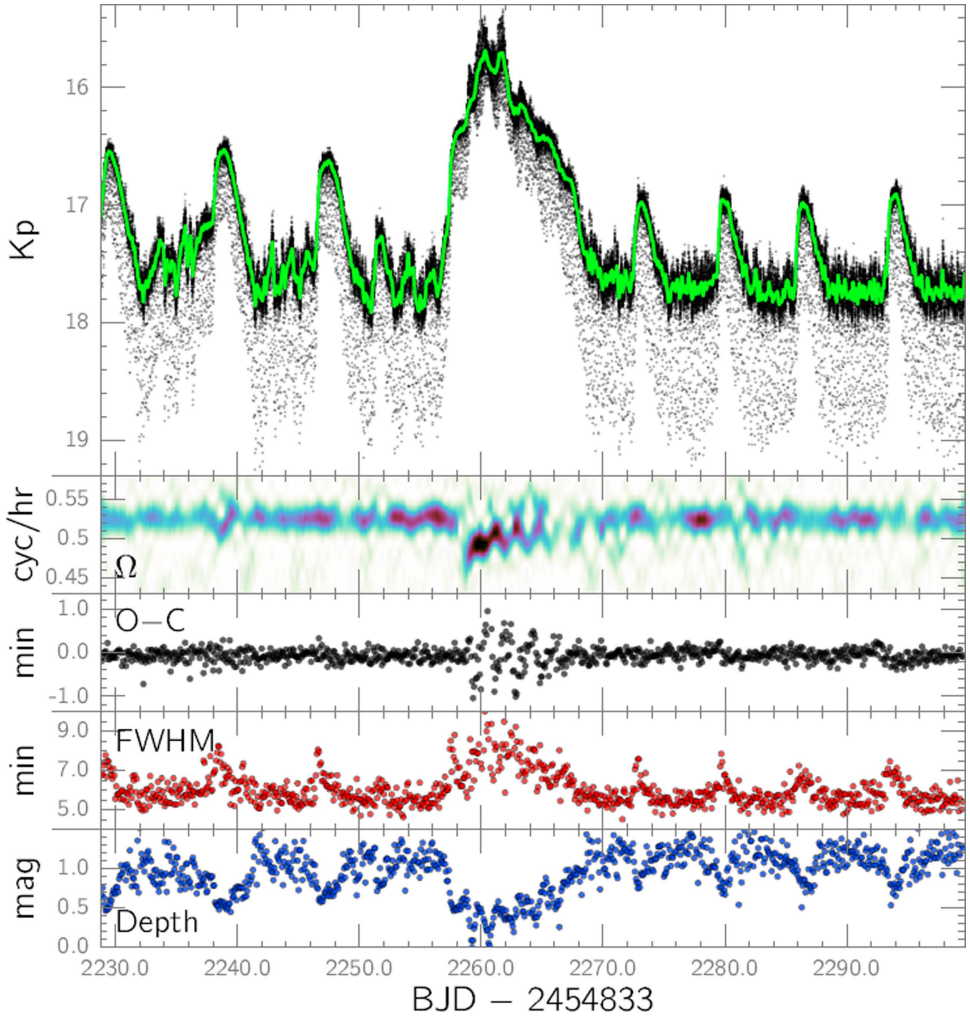


Figure 3. Top panel: the full *K*2 light curve of J0359. The smoothed light curve is superimposed as a green line. Minioutbursts give rise to the choppy appearance of the three quiescent segments prior to the superoutburst. From top to bottom, the remaining four panels show the trailed power spectrum around the orbital period's fundamental harmonic (Ω), the eclipse O–C, the eclipse full width at half minimum, and the eclipse depth. The normal outbursts shift the mid-eclipse times to earlier phases because the increased disk luminosity moves the centroid of disk emission away from the hot spot and toward the disk center.

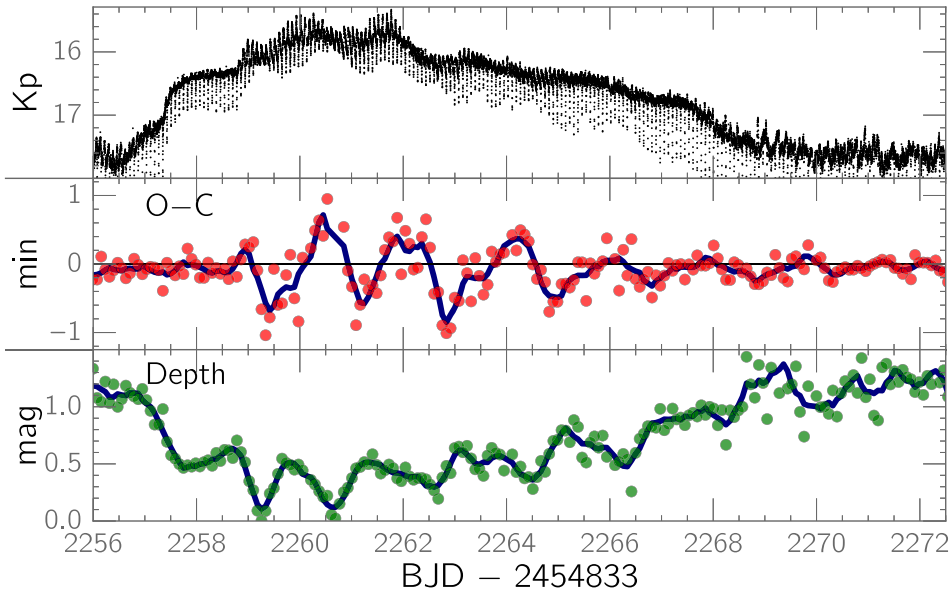


Figure 4. Behavior of the eclipse O–C timings and depth during the superoutburst. These data were also shown in Figure 3, but we enlarge them here so that details may be more readily discerned.

Table 2
The Parameters from Fitting Equation (3.1) to Each of the Visible Outbursts

Outburst	Start Date (BJD)	Duration (days)	Time Between Outbursts (days)[a]	Amplitude[b]	Rise Time (days)	Decay Time (days)
1	2457061.91(8)	2.51(8)	...	2.6(1)[c]	>0.56[d]	1.96(8)
2	2457071.02(8)	2.90(8)	9.12(8)	2.8(1)[c]	0.92(8)	1.98(8)
3	2457079.38(8)	3.20(8)	8.36(8)	2.3(1)	1.15(8)	2.05(8)
4 (SU)	2457089.94(8)	1.86(8)	10.56(8)	3.2(1)	1.73(8)	...
5	2457105.48(8)	2.12(8)	15.54(8)	2.0(1)	0.74(8)	1.37(8)
6	2457112.41(8)	2.24(8)	6.93(8)	1.9(1)	0.55(8)	1.69(8)
7	2457118.78(8)	2.24(8)	6.37(8)	2.0(1)	0.50(8)	1.75(8)
8	2457126.21(8)	2.31(8)	7.42(8)	2.2(1)	0.86(8)	1.44(8)

Notes. The superoutburst parameters (SU in the table) represent the parameters for the precursor of the superoutburst. Due to the strong orbital variations in the light curve caused by the bright spot and eclipse, we have taken the error in the timing measurements to be the length of a single orbit.
[a] The time between outbursts is defined as the time between the start of the given outburst and the start of the previous outburst. Because of this, outburst 1 does not have a value.
[b] Amplitudes are expressed as flux ratios between the maximum flux during outburst and the pre-outburst quiescent flux.
[c] The amplitudes of these outbursts were calculated using the quiescent flux after the outburst had ended. This was due to the lack of a quiescent level before outburst 1 (as the outburst was rising at the start of the exposure) and due to an abnormally high pre-outburst level for burst 2 (see the top panel of Figure 7).
[d] We can only provide a lower bound for the rise time of the burst, as outburst 1 started before the beginning of the *K*2 observations.

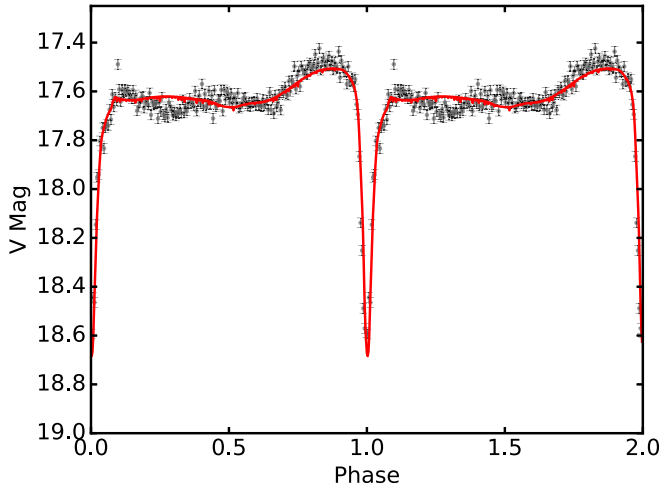


Figure 5. A parameterized model (red line) of the quiescent light curve using the Orosz & Hauschildt (2000) code, yielding a firm constraint of $i = 77° \pm 2°$.

vary, we searched for the best-fit parameters using a Monte Carlo Markov Chain. While many of the model parameters were unconstrained, the inclination was tightly constrained to $i = 77° \pm 2°$. The uncertainty was found by measuring changes in the χ^2 value based on the number of free parameters, but given that so many other parameters are unconstrained, it is possible that this nominal uncertainty might be underestimated.

3.1. Normal Outbursts

There are a total of eight normal outbursts in the *K*2 data, including the precursor normal outburst. Table 2 lists the details of these outbursts, and Figure 6 overlays each of the normal outbursts so that their amplitudes and shapes may be compared. They were modeled using a pair of Gompertz functions such that the rise and fall could be described by separate Gompertz functions, joined in the middle. The function describing the flux took the form

$$F(t) = \begin{cases} a_1\, e^{-e^{-k_1(t-t_1)}} + c_1, & \text{for } t \leqslant t_0 \\ a_2\, e^{-e^{-k_2(t-t_2)}} + (c_1 + a_1), & \text{for } t \geqslant t_0 \end{cases}$$

Here, a_1 and a_2 are the amplitude of the rise and fall of the outburst; k_1 and k_2, respectively, control how fast the rise and fall of the outburst were; c_1 is the quiescent level before the outburst; t_1 is the mid time of the rise; t_2 is the mid time of the fall; and t_0 is the time at which the function transitions from rising to falling. Allowing different a_1 and a_2 values for a single outburst enables the quiescent brightness to change after the outburst. Table 2 lists the model parameters obtained by fitting this function to each normal outburst, and Figure 7 shows a representative fit to one of the outbursts.

The parameters in Table 2 show that before the superoutburst, the amplitude of the normal outbursts was ~0.4 mag larger, and the fade to quiescence took about a half-day longer. Moreover, the fast rise times and comparatively slow decay rates indicate that the outbursts originated in the outer disk and moved inward. The behavior of the eclipse width, which reached a maximum almost immediately after the onset of the normal outbursts, supports this interpretation. An outburst starting in the outer disk will cause an immediate jump in the eclipse width because the donor star cannot eclipse the entire outbursting region of the disk. By contrast, in the early stages of an inside-out outburst, the outburst luminosity would be confined to the inner disk, which would be eclipsed more quickly and more completely than the outer disk, resulting in deeper, narrower eclipses (Webb et al. 1999).

During some of the normal outbursts (particularly the sixth and eighth normal outbursts), the time of eclipse minimum occurred up to ~15 s earlier than in quiescence (Figure 3). This phenomenon probably resulted from the diminished relative contribution of the hot spot to the overall light curve during an outburst. Because the hot spot is eclipsed after the center of the disk, the eclipses will occur later if the hot spot is dominant, as is the case during quiescence. During outburst, the disk becomes more luminous than during the quiescent state, so the

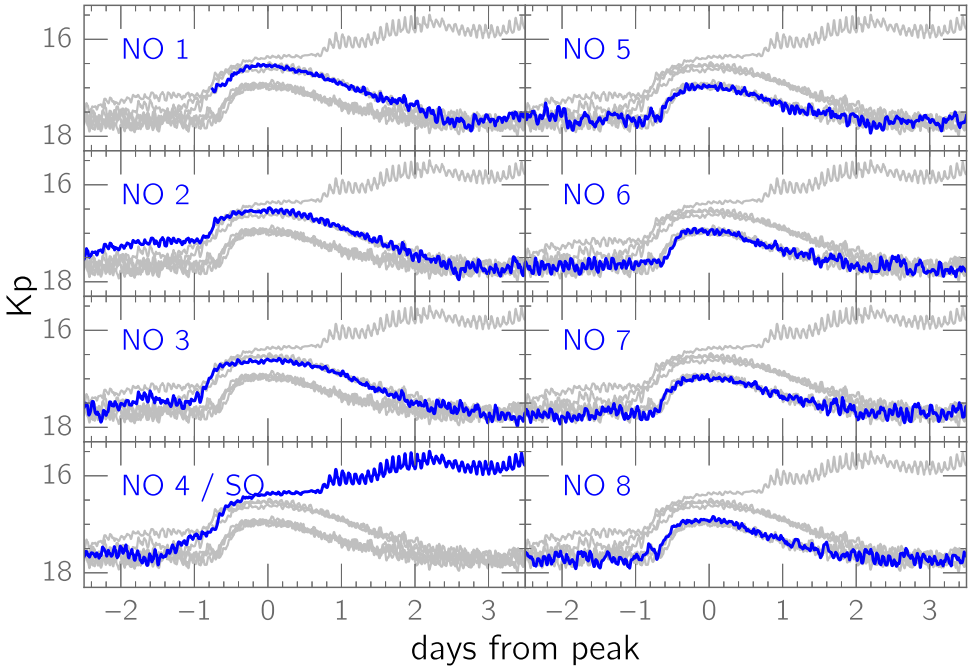


Figure 6. An overlay of smoothed light curves of the normal outbursts. The peak of each outburst is centered on $t = 0$ days, and each panel highlights a different normal outburst. Before the superoutburst (left column), there was scatter in the peak brightnesses of the different outbursts, and the quiescent level prior to outburst was variable as well. After the superoutburst (right column), the normal outbursts peaked at similar magnitudes, had comparable rise and decline times, and showed similar quiescent magnitudes in the lead-up to the outburst. The precursor of the superoutburst was brighter than the other normal outbursts, and it was still brightening at the same time that the other outbursts were declining.

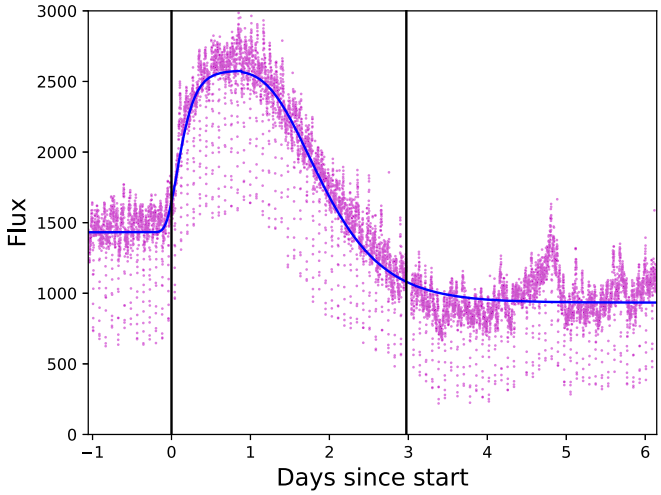


Figure 7. The result of fitting Equation (3.1) (blue) to the second outburst in the *K*2 light curve (magenta). The black lines denote the times at which the model flux reach 1.15 times the value of the constant level. The pre-outburst flux level before the outburst was much higher than the quiescent level afterwards.

disk's centroid of emission is eclipsed at an earlier orbital phase (Ramsay et al. 2017).

The properties of eclipses during the normal outbursts change after the superoutburst, becoming narrower in FWHM by ∼30 s and deeper by several tenths of a magnitude. These observations imply that the maximum radius of the disk during outburst was smaller after the superoutburst, a key prediction of the TTI model. Although we attempted to use the ELC code to quantitatively measure the change in disk radius, there were too many free parameters to achieve a reliable measurement.

3.2. Precursor Outburst

At approximately BJD 2457090.37, J0359 initiated a precursor normal outburst that subsequently triggered a superoutburst. The rise to precursor maximum took approximately 0.7 days, and the superhumps appeared an additional ∼0.7 days thereafter, a total of ∼18 orbital cycles from the start of the precursor.

Compared with the three previous normal outbursts, the precursor was ∼0.2 mag brighter at maximum light, and whereas the other outbursts declined after reaching peak brightness, the precursor plateaued after its maximum. Immediately after the precursor's peak, the eclipse FWHM began to decline and the eclipse depth increased, exactly as was observed in the other normal outbursts (Figure 3). Both effects are consistent with the inward propagation of a cooling front, but the lack of a concomitant fade in the overall brightness implies the presence of an additional mechanism to offset the cooling front's reduction of the disk luminosity.

Moreover, in the three orbits prior to superhump onset, the hot spot was no longer discernible. During these orbits, there were several prominent dips of unknown origin, and the overall brightness gradually increased by ∼0.1 mag.

3.3. Superoutburst Light Curve

The first superhump appeared at BJD ∼ 2457091.82, at which time the light curve immediately began rising to superoutburst maximum. Once the superhumps appeared, their development was very rapid, and by the third superhump cycle, their amplitude had already reached its maximum value of 0.4 mag (Figure 8, lower panel). The superhump amplitude might have been even larger, but the superhumps and eclipses beat against each other, distorting the profiles of many superhump maxima. The rise to superoutburst maximum lasted

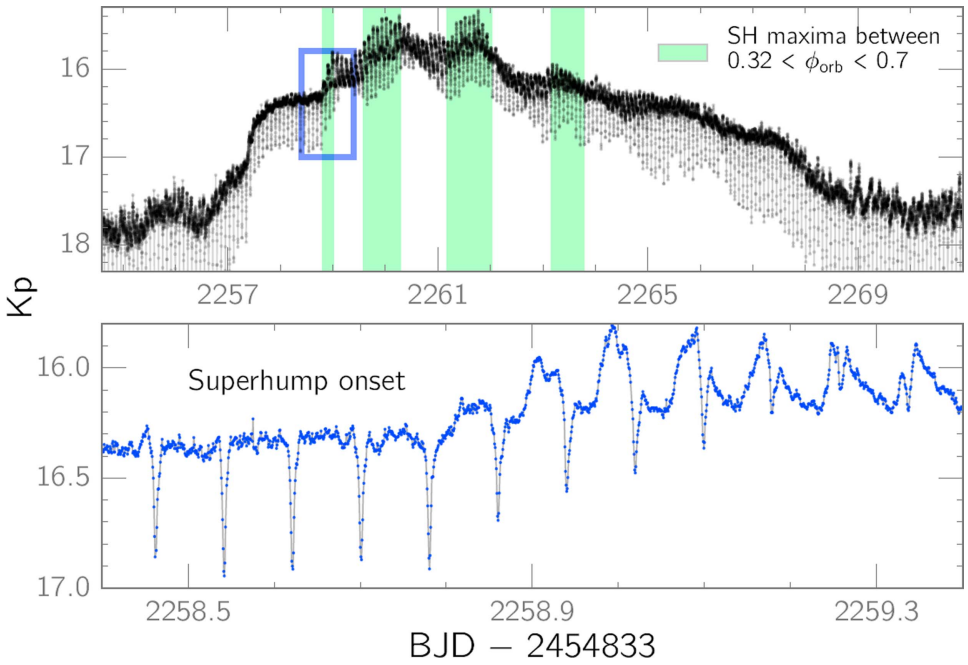


Figure 8. The light curve of the superoutburst. The segment enclosed by the rectangle indicates where superhumps appeared, and the bottom panel shows an enlarged view of this segment of the light curve. The highlighted regions indicate parts of the superoutburst during which the superhump amplitude was largest, and as discussed in the text, there is an orbital-phase dependence to this phenomenon.

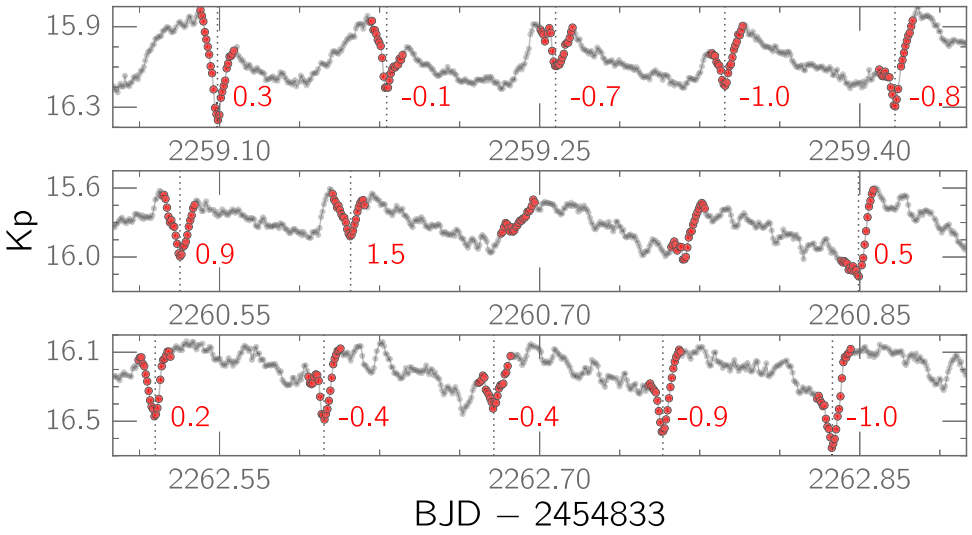


Figure 9. Light curves showing three different times at which the eclipses coincided with the superhump maxima. The red, enlarged points denote data obtained between $0.9 < \phi_{orb} < 1.1$, and the red number next to each eclipse is the O–C timing residual for mid-eclipse, given in minutes. The dotted vertical lines indicate the measured time of minimum light. No value is given for two eclipses in the middle panel because those eclipses are essentially indistinguishable from the superhump profile.

until BJD ∼ 2457093.3, although the presence of eclipses and superhumps makes it difficult to reliably discern the exact time at which the superoutburst peaked.

During the superoutburst, the eclipse O–C timings (Figure 4) showed oscillations when the eclipses lined up with the superhump light source. Figure 9 shows three segments of the superoutburst light curve during which the eclipses occurred at superhump maximum. For example, when the eclipses and superhump maxima coincided during the initial rise to superoutburst maximum, mid-eclipse occurred approximately one minute earlier than predicted by the orbital ephemeris (top panel in Figure 9). This implies that the superhump light source was located in the trailing half of the disk. Later, near BJD ∼ 2457093.8, two consecutive eclipses were so shallow that they could not be readily distinguished from the superhump profile, implying a grazing eclipse of the superhump light source.

Another noteworthy aspect of the superoutburst is that it contained several shallow fading events during which the overall brightness decreased by several tenths of a magnitude. These dips can be seen in the gaps between the four highlighted regions in the top panel of Figure 8. The fades lasted for about one day, and each was centered on the time that the eclipses coincided with the superhump maxima.

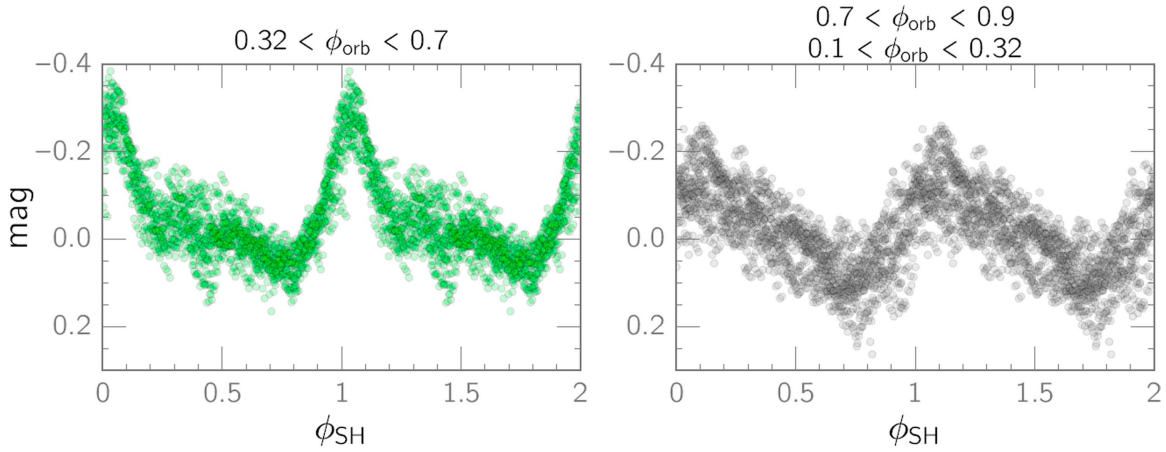


Figure 10. Reconstructed profiles of Stage B superhumps between BJD 2457092.8−2457096.0, when the superhump period was stable at 2.003 hr. We built the profiles using the detrended light curve described in the text, and then filtered the data by orbital phase. Superhumps observed between orbital phases 0.32–0.7 had a sharper profile and larger amplitude than those observed at other orbital phases. Observations between orbital phases 0.9–1.1 were excluded from these plots because of unavoidable eclipse contamination.

The fading events showed a strong dependence on the orbital phase at which the superhump maximum occurred. After subtracting the smoothed light curve to isolate the pulsed flux, we constructed two phase plots of the Stage B superhump profile, when the superhump period was constant at 2.003 hr. The first phase plot used only data obtained between $0.32 < \phi_{orb} < 0.7$, which, from visual inspection of the light curve, we estimated to be the orbital phases during which the superhump maximum was the brightest and most clearly defined. The second phase plot of the superhump used data from all remaining orbital phases (except $0.9 < \phi_{orb} < 1.1$, as these phases are inevitably contaminated by eclipses). The resulting phase plots are shown in Figure 10. The reconstructed superhump profile for $0.32 < \phi_{orb} < 0.7$ is sharper and has a higher amplitude than the noisy superhump profile for the remainder of the data.

There are at least two possible explanations for this phenomenon. Osaki & Meyer (2003) calculated that in high-inclination systems, the strength of the superhump signal will depend on the orbital phase at which the superhump occurs. According to their work, about half of the superhump light originates in the vertically extended rim of the disk, the visibility of which will vary across the orbital cycle when the disk is seen edge-on. In their Figures 2 and 3, they predict that superhump maxima will be strongest for about half of an orbit centered on an orbital phase of ∼0.75, mimicking the orbital hump from the stream-disk hot spot. This differs from the orbital phases (0.32–0.70) at which we observed the highest-amplitude superhumps in J0359.

Another possible cause of the fades is obscuration of the inner disk by vertically extended disk structure at certain orbital phases. In this scenario, the superhump light source would have been partially obscured except when it occurred between $0.32 < \phi_{orb} < 0.7$. Billington et al. (1996) reported evidence of such structure in the eclipsing system OY Car, in which the optical superhump maxima corresponded with deep ultraviolet dips. Furthermore, Murray (1998) predicted that the temperature gradient of a superhumping disk could be capable of producing azimuthal variations in the height of the disk rim.

3.4. Period of Stage A Superhumps

To measure the period of Stage A superhumps, we performed an O–C analysis (Figure 11) by fitting the superhump maxima with polynomials and extracting the time of maximum light. All observations between $0.9 < \phi_{orb} < 1.1$ were excluded to reduce the effect of the orbital modulation. A robust Theil–Sen linear fit to the timings of the Stage A maxima shows the superhump period to have been constant at 2.089 ± 0.007 hr before an abrupt jump to a 2.003 hr period, consistent with a transition from Stage A to B superhumps. Five of the ten stage A superhumps were adulterated by eclipses, so their maxima were not included in the analysis. To quantify the timing uncertainties on individual maxima, we performed 100 simulations in which we repeated the fitting procedure after randomly selecting half of the data points that had been used to fit each individual superhump. We then used a Monte Carlo simulation to estimate the uncertainty of the Stage A period.

We also calculated Lomb–Scargle and phase-dispersion-minimization (PDM; Stellingwerf 1978) periodograms for Stage A after subtracting the smoothed light curve (Figure 3) to detrend the data. We excluded observations between $0.9 < \phi_{orb} < 1.1$ after determining that their inclusion systematically inflated the measured period of Stage A. Using two harmonic terms, the Lomb–Scargle analysis yielded a period of 2.076 ± 0.005 hr, while the period in the PDM periodogram was 2.078 ± 0.005 hr. These periodograms are shown in Figure 11. To estimate the 1σ uncertainties, we used a method similar to one from Kato et al. (2012). We performed the Lomb–Scargle and PDM analyses on 100 random subsets, each of which contained half of the observations during Stage A, and we derive the uncertainties from the resulting distributions.

We caution, however, that the overlap between eclipses and superhump maxima can bias the measured period of Stage A, corrupting the computed mass ratio (as occurred during the 2010 superoutburst of HT Cas; Kato & Osaki 2013). Of the three methods that we used, the O–C analysis of the polynomial fits to the superhump maxima is probably the most vulnerable to this problem, so we excluded Stage A maxima that fell between $0.9 < \phi_{orb} < 1.1$. As the Lomb–Scargle and PDM periodograms use the full superhump profile—and not

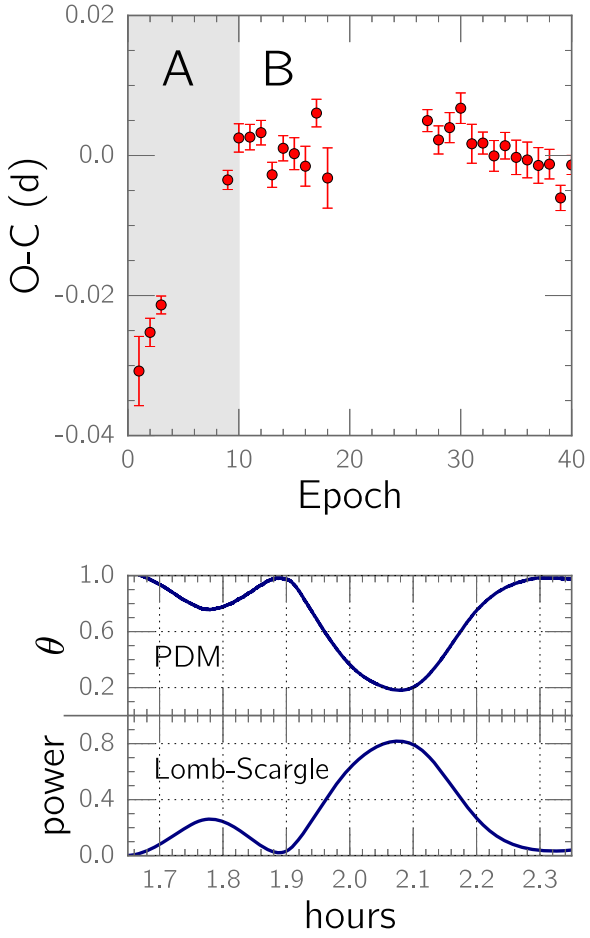


Figure 11. Top panel: an O–C diagram of the Stage A–B superhump transition, showing a Stage A period of 2.089 ± 0.007 hr. The times of maxima were measured by fitting superhumps with polynomials, and maxima between $0.9 < \phi_{\rm orb} < 1.1$ are not plotted because of eclipse contamination. Bottom panel: PDM and Lomb–Scargle periodograms of Stage A, yielding periods of 2.076 ± 0.005 hr and 2.078 ± 0.005 hr, respectively. Before they were computed, observations between $0.9 < \phi_{\rm orb} < 1.1$ were excluded, and the light curve was detrended. Candidate periods are minima with PDM and maxima with Lomb–Scargle.

just the maximum—they might be less susceptible to distortions in the profiles of individual superhump maxima.

In Section 5.1, we use these three estimates of the Stage A period to calculate the corresponding binary mass ratio.

3.5. Phase Shift of the Hot Spot

Using the detrended light curve, we created phase plots of the quiescent orbital modulation before and after the superoutburst. A comparison of these plots, shown in Figure 12, reveals that the hot spot shifted toward earlier orbital phases after the superoutburst. The significance of this effect is discussed in Section 5.2.

4. Spectroscopy

The 2015–2016 LBT and 2014–2015 APO spectra were largely comparable, except for minor variations in the continuum slope. All spectra showed double-peaked Balmer and He I emission lines from the disk, with the centers of the He I lines dipping below the continuum into absorption (Figure 13). There was also weak He II λ4686 Å emission.

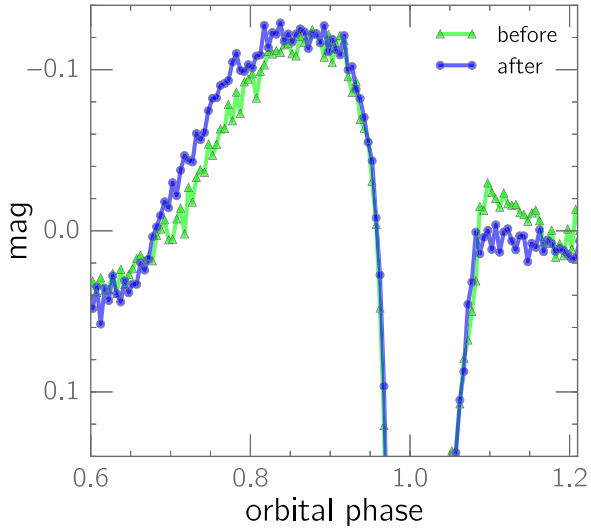


Figure 12. A phased light curve of the hot spot, before and after the superoutburst. Before the data were phased, they were detrended by subtracting a smoothed light curve. The bin width for each point is 0.005 phase units. The orbital hump shifted toward earlier phases after the superoutburst, as did the hot spot's egress feature.

O I λ7774 Å was seen in absorption with a FWHM of ∼500 km s^{-1}, exhibiting radial-velocity variations on the orbital period. Its phasing suggests an origin within the disk, and unlike the disk emission lines, it disappeared entirely during the eclipse.

We constructed Doppler tomograms from the Hα and Ca II λ8662 Å lines in the 2016 LBT data using code by Kotze et al. (2015), and we show them in Figure 14. Both tomograms are dominated by the stream-disk hot spot, and the Ca II tomogram also shows weak emission from the donor.

4.1. Radial Velocity of the Donor Star

Emission from the donor star was detectable in the Ca II λ8542 Å and λ8662 Å lines, but the former overlapped with emission from another Ca II line. Thus, we used the λ8662 Å line to characterize the orbital motion of the donor. A trailed spectrum of this line shows double-peaked emission from the disk with a partial S-wave superimposed. The phasing of the S-wave, with maximum redshift at $\phi_{\rm orb} = 0.25$ and maximum blueshift half a cycle later, clearly indicates that it originated on the donor. The S-wave was apparent (albeit weakly) for only half of the orbit before it became overwhelmed by disk emission. Although we searched for additional spectral lines from the secondary, such as the near-infrared K I and Na I absorption doublets, we detected only the two Ca II lines.

We used two methods to constrain the semiamplitude (K_2) and systemic velocity (γ) of the donor based on the Ca II emission. First, we visually fitted a sinusoid with a period of 1 to the trailed spectrum, adjusting K_2 and γ to achieve a satisfactory fit. Second, we applied a two-dimensional cross-correlation of the trailed spectrum, with the template being half of a sine wave with a fixed period of 1. We iterated across a range of plausible values for K_2, rebuilding the template for each such value. Both methods agree that $K_2 \approx 320$ km s^{-1} and $\gamma \approx 20$ km s^{-1}. We do not have formal 1-σ uncertainties for these values, but we visually estimate uncertainties of ±20 km s^{-1} for both K_2 and γ.

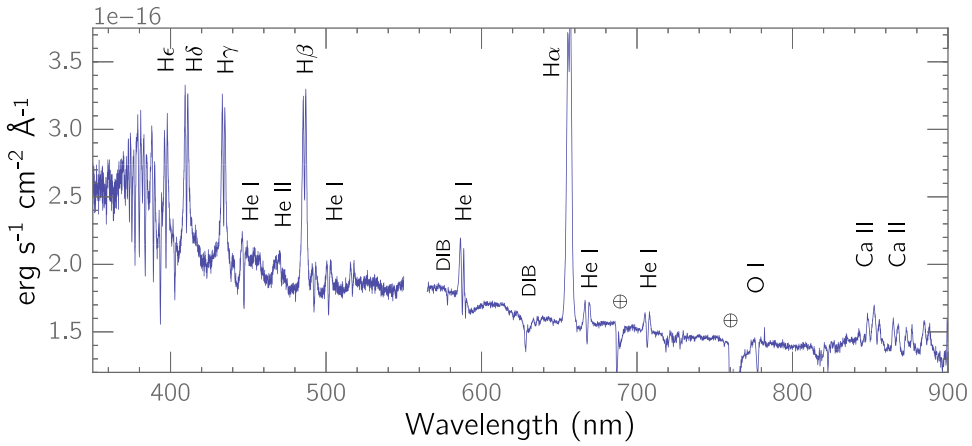


Figure 13. Average spectrum of J0359 in 2016, with major lines identified. "DIB" refers to diffuse interstellar bands. The Balmer lines blueward of Hδ and the He I lines all show central absorption components. O I λ777 nm is seen in absorption. The gap near 560 nm is due to a dichroic that splits the light into the two MODS spectrographs. No velocity correction has been applied.

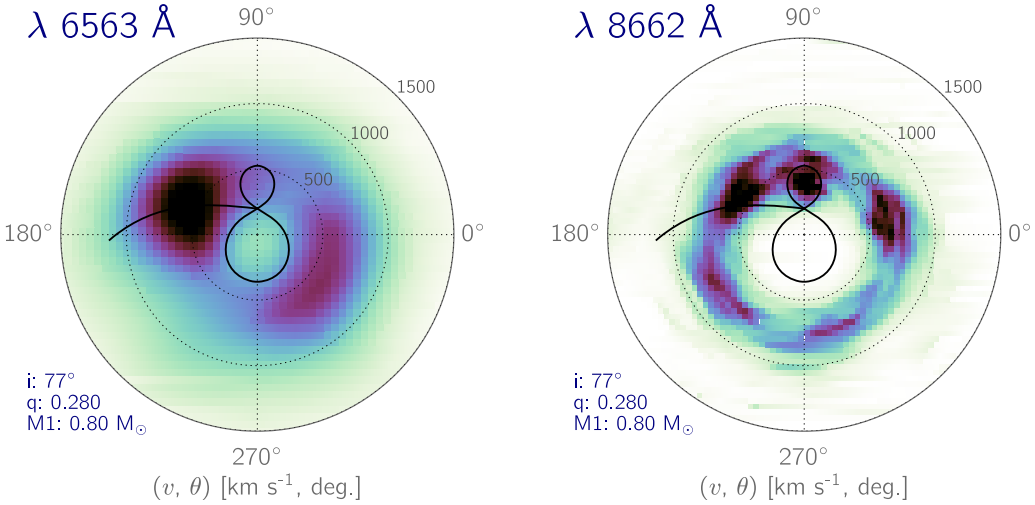


Figure 14. Doppler tomograms of Hα (left) and Ca II (right). The WD mass has been assumed. Emission from the donor was present only in the Ca II lines. The Roche lobes corresponding to $q = 0.28$ have been plotted, as has the ballistic trajectory of the accretion stream.

A limitation of this method is that it assumes that the observed emission tracks the donor's center of mass. In reality, there is no such guarantee, as different regions on the donor will have different orbital speeds, depending on their location within the donor's Roche lobe. The absence of the donor's emission lines during the eclipse shows that the lines were produced on the donor's inner hemisphere, most likely as the result of irradiation of regions that were unshielded by the accretion disk. Consequently, the observed donor-star emission probably originated somewhere between the L1 point and the secondary's center of mass, in which case our measurement of K_2 underestimates the true value for the donor.

4.2. Radial Velocity of the Disk

We estimated the disk's velocity variations in the LBT data by using the "double-Gaussian" method developed by Shafter (1983). The method consists of convolving an emission line with two Gaussian functions separated in wavelength. The wavelength at which the Gaussian functions contain equal flux is an estimate of the velocity centroid of the emission from the inner disk, approximating the motion of the WD. We used a Gaussian sigma of 7 Å, which is typical for this analysis. We analyzed the bright, uncontaminated H_α and H_β emission lines, and their velocities were fitted to the function

$$V(t) = -K_1 \sin\left(\frac{2\pi(t - t_0)}{P} + \phi_0\right) + \gamma, \quad (1)$$

with the free parameters of WD velocity amplitude (K_1), velocity offset (γ), and phase (ϕ). We fixed the orbital period (P) to that derived from the $K2$ photometry. This process was repeated for a range of Gaussian separations until the parameters that provided the minimum velocity scatter were found. The velocity estimates made around the eclipse were dominated by the Rossiter–McLaughlin effect, so their errorbars have been inflated to avoid strongly influencing the velocity fits.

Application of the double-Gaussian method to the H_α emission (Figure 15) results in $K_1 = 123 \pm 4$ km s^{-1} and $\gamma = 43 \pm 3$ km s^{-1}. The offset in phase between the best-fit sinusoid and the time of eclipse is $\phi_0 = 0.12 \pm 0.01$ (Figure 16). The same analysis applied to the H_β emission yields $K_1 = 129 \pm 5$ km s^{-1} and $\phi_0 = 0.12 \pm 0.02$, consistent with the H_α results.

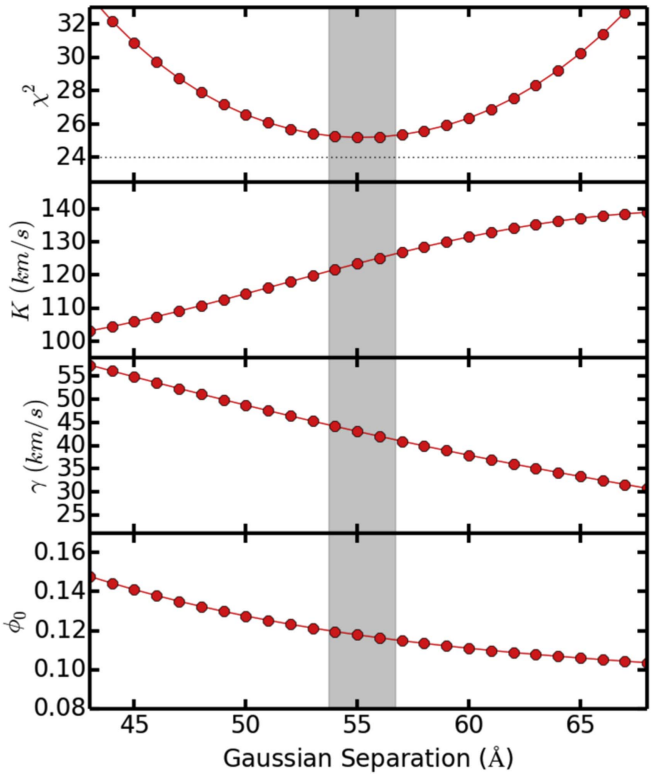


Figure 15. The double-Gaussian method applied to the H_α emission feature, showing that the lowest scatter occurs for a Gaussian separation of 55 Å. The velocity amplitude and center of mass velocity vary slowly with the separation parameter. The time of zero radial velocity shows a significant offset from the time of the photometric eclipse with $\phi_0 = 0.12$.

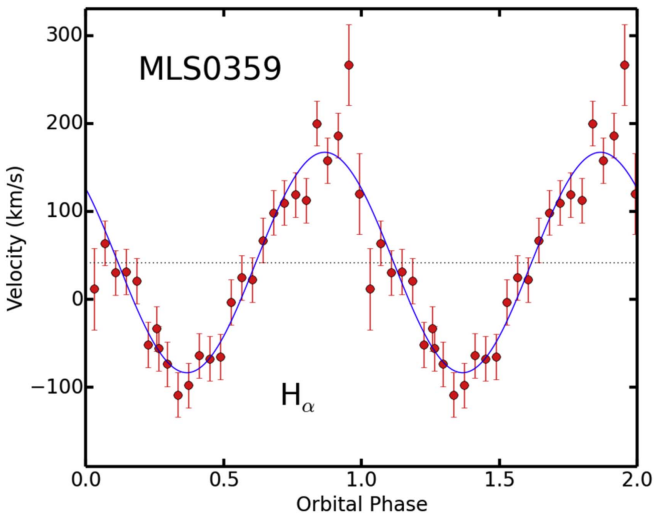


Figure 16. Radial velocity curve of the inner disk, approximating the motion of the WD. The orbital phase is based on the time of the photometric eclipse. The three spectroscopic measurements during eclipse have been discounted from the radial velocity fit by inflating their uncertainties.

The time-resolved APO spectra yield similar values, showing the disk to be relatively stable over timescales of years.

5. Discussion

5.1. Mass Ratio

There is a fundamental relationship between a CV's mass ratio ($q = \frac{M_2}{M_1}$) and its ability to develop superhumps. The TTI model predicts that superhumps form when the outer disk achieves a 3:1 resonance with the donor star, but if the mass ratio is too high, tidal forces from the secondary truncate the disk before it can reach this size. In simulations, superhumps do not appear if $q \gtrsim 0.25$ (Smith et al. 2007).

As discussed in Section 1, Kato & Osaki (2013) proposed that the period of Stage A superhumps is equivalent to the dynamical precession rate at the 3:1 resonance, meaning that the mass ratio can be very accurately determined by measuring the fractional excess ($\epsilon^* = 1 - \frac{P_{\rm orb}}{P_{\rm sh}}$) of Stage A superhumps. In Section 3.4, we used three different techniques to measure the period of Stage A, obtaining three estimates of the period. For each, we measured ϵ^* using the orbital period of 1.909 hr and applied Equation (1) in Kato & Osaki (2013) after correcting for a misprint (Kato et al. 2016, footnote 5).

The O–C, PDM, and Lomb–Scargle periods were 2.089 ± 0.007 hr, 2.078 ± 0.005 hr, and 2.076 ± 0.005 hr, respectively, and the corresponding period excesses result in mass ratios of 0.298 ± 0.016, 0.275 ± 0.011, and 0.270 ± 0.011. These uncertainties assume that the uncertainty on each period is the standard deviation of a Gaussian distribution whose mean is the measured period. The average of these mass ratios is $q = 0.281 \pm 0.015$, where the uncertainty is the rms of the three estimates of the mass ratio. This value is marginally inconsistent with the theoretically predicted threshold of $q = 0.25$ for superhump development, though we reiterate that the contamination of Stage A superhump maxima by eclipses can potentially lead to an inaccurate measurement of the Stage A period (Kato & Osaki 2013). At the very least, J0359 is very close to $q = 0.25$, but it will take an independent measurement of the mass ratio to conclusively establish whether $q > 0.25$.

Because we have estimated K_1 and K_2 from the spectra, we have a second means of nominally estimating the mass ratio. For $K_1 = 123\,{\rm km\,s^{-1}}$ and $K_2 = 320\,{\rm km\,s^{-1}}$, the mass ratio would be $q = 0.38$. However, it is likely that there are systematic errors impacting both values. Given the caveats described earlier, our value for K_2 is probably a lower limit for the true orbital motion of the secondary. Moreover, as Long & Gilliland (1999) showed, estimates of K_1 from the line wings can deviate significantly from the true orbital motion of the WD. While there is insufficient data to obtain a reliable dynamical estimate of the mass ratio, the large changes that are needed to satisfy $q = \frac{K_1}{K_2} \simeq 0.25$ furnish modest support for the high mass ratio implied by the superhump method.

Although Murray et al. (2000) identified a scenario in which superhumps could develop in systems with mass ratios as high as $q = 0.33$, their proposal requires the mass-transfer rate to abruptly plummet (e.g., as in VY Scl stars). However, the closely spaced outbursts in J0359 require a fairly high and stable mass-transfer rate, so their theory is not applicable to the case of J0359.

J0359 is at least the third system in which the Stage A method yields a mass ratio in excess of $q = 0.25$, the other two being V1006 Cyg (Kato et al. 2016) and MN Dra (Kato et al. 2014). The fact that the Stage A method yields a mass ratio above $q = 0.25$ for these systems suggests that either the period of Stage A superhumps is not purely dynamical (in contradiction of Kato & Osaki 2013) or that the disk can become eccentric at mass ratios higher than predicted by simulations (in contradiction of simulations; e.g., Smith et al. 2007). As our referee, Taichi Kato, pointed out to us,

the first option is unlikely; the pressure effect that causes the superhump period to shorten during Stage B decreases the disk's precessional rate, so if it were present during Stage A as well, the result would be a shorter Stage A period—and, therefore, a lower mass ratio. Conversely, smoothed-particle-hydrodynamics simulations of disks generally do not model the disk-instability mechanism or the resulting changes in the disk's radius, raising the possibility that the 3:1 resonance may be achieved more easily than these simulations predict.

5.2. Shrinkage of the Disk After the Superoutburst

One of the core predictions of the TTI model is that the radius of the accretion disk gradually increases across a supercycle, with a minimum radius after the superoutburst (Osaki 1989). The behavior of the stream-disk hot spot in J0359 provides evidence of this phenomenon.

As discussed previously in Section 3.5 and shown in Figure 12, the hot spot shifted toward earlier orbital phases after the superoutburst. We computed the coordinates within the binary rest frame of the stream-disk collision, assuming a ballistic trajectory from the L1 point for $q = 0.28$, for different values of the disk radius between $0.25a$ and $0.4a$, where a is the orbital separation.[7] The schematic diagram in Figure 17 shows that as the disk radius shrinks, the hot spot is viewed most directly at earlier orbital phases. For example, if the disk radius were to shrink from $r = 0.4a$ to $0.3a$, the hot spot would be seen face-on $\sim$0.03 phase units earlier.

Using the coordinates of the stream-disk collision at different disk radii, we calculated the orbital phases at which that point would undergo eclipse ingress and egress. We find that as the disk radius expands, the eclipse of the hot spot becomes longer and ends later. Thus, a shrinkage of the disk radius after the superoutburst could account for the observed decrease of the eclipse duration.

Moreover, the changed location of the hot spot resulted in a significant change in its appearance after the eclipse. Prior to the superoutburst, the declining edge of the hot spot was visible after the eclipse, but this feature disappeared after the superoutburst. The most straightforward interpretation is that disk radius shrank after the superoutburst, enabling the stream to travel farther along its ballistic trajectory before striking the disk. In principle, this change should also lead to an increased luminosity of the hot spot after a superoutburst, as the stream-disk collision is deeper in the WD's gravitational potential. This effect would probably be far easier to detect in a non-eclipsing system, as the presence of eclipses greatly complicates efforts to identify changes in the spot's luminosity.

5.3. Superhump Growth Rate

As stated in Section 3.3 and shown in Figure 8, the superhumps in J0359 became apparent only $\sim$18 cycles after the start of the precursor outburst and only $\sim$9 cycles after the precursor's maximum. These short times are consistent with Lubow (1991a, 1991b) who calculated that growth rates to reach the 3:1 resonance should be proportional to q^2. At the low q values typically observed in very short-period SU UMa systems, the appearance of superhumps takes about 60 cycles for $q = 0.06$, so the faster time for the higher q of J0359 is expected. The Stage A duration of 9–10 cycles is in accord with a high value of q, as shown from the compilation in Kato et al. (2015).

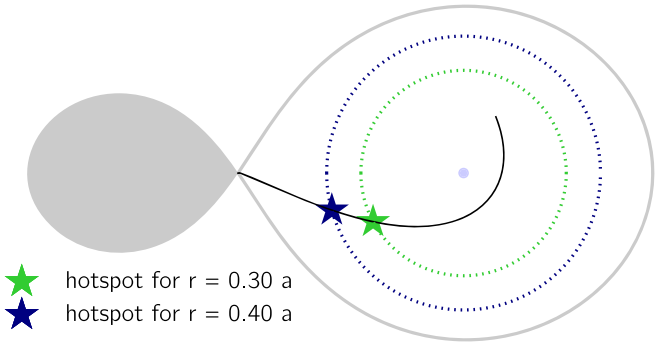


Figure 17. Roche geometry for MLS, with the ballistic trajectory of the accretion stream plotted as a black line. For two different disk radii, the point of collision between the stream and the outer rim of the disk (dashed lines) is shown.

However, the fast rise of Stage A and its short duration do not agree with the values for the high-q ($\geqslant$0.26) system V1006 Cyg (Kato et al. 2016), which took about 30 cycles for the superhumps to appear and in which Stage A lasted for at least 32 cycles. MN Dra also appears to have a large q value (0.29) and a long Stage A (Kato et al. 2014). Kato et al. (2016) postulated that systems with mass ratios near the tidal-stability limit might have slow superhump growth rates. Both the MN Dra and V1006 Cyg data sets suffered from lack of data at the start of the outburst, and both systems have somewhat peculiar orbital periods in the period gap, so it will require further data on high-q systems to determine how superhump development is affected by a high mass ratio.

5.4. Minioutbursts

During the best-defined minioutburst, the eclipse depth increased, as did the FWHM, consistent with the extra luminosity originating in the outer disk. If the minioutbursts originated in the inner disk or on the WD, the eclipses would have immediately become deeper and narrower. The minioutbursts ceased in the wake of the superoutburst, implying that their appearance was closely linked to disk changes during the supercycle or to accretion episodes that ended after the superoutburst.

Osaki & Kato (2014) reported the detection of minioutbursts in *Kepler* observations of V1504 Cyg and proposed that they were related to the increased disk radius during the supercycle. Specifically, they argued that tidal dissipation in the outer disk could prematurely trigger a thermal instability, causing a brief outburst with a diminished amplitude. In their explanation, the disk then jumps from the cold branch of the thermal equilibrium curve to an intermediate warm branch (as opposed to the hot branch, as would occur during a normal outburst). Because the TTI model predicts that the disk radius will increase during the supercycle, it offers a plausible explanation as to why the minioutbursts in J0359 are only observed before the superoutburst. A theoretical examination of this proposal would be a logical next step.

It is also possible that a beat phenomenon between the orbital signal and failed superhumps could produce the minioutbursts. Failed superhumps are observed during the declining portion of normal outbursts before a superoutburst and fall into two general categories—positive and negative—depending, respectively, on

[7] These calculations treat the hot spot as a point-source on a perfectly circular disk rim that is eclipsed by a spherical donor star.

whether their period is longer (Osaki & Meyer 2003) or shorter (Osaki & Kato 2013, and references therein) than the orbital period.

Because the maxima of the minioutbursts occur quasi-periodically every ∼2 days, the 1.909 hr orbital period would need to beat against a periodicity of roughly ∼1.84 hr (0.545 cycles hr^{-1}) or ∼1.99 hr (0.503 cycles hr^{-1}), as $\nu_{beat} = |\nu_{orbit} - \nu_{SH}|$. In the trailed power spectrum in Figure 3, there is a brief (∼0.5 days) oscillation near the peak of the second normal outburst, during which the power shifts from the orbital period to a period of ∼1.96 hr. As this is longer than the orbital period, this could be attributable to failed positive superhumps, which are thought to arise when a normal outburst is extinguished before the tidal instability has had enough time to fully develop in disk material at the 3:1 resonance radius (Osaki & Meyer 2003). According to Osaki & Meyer (2003), this underdeveloped tidal instability should not persist into quiescence in a high-mass-ratio system, making it difficult to envision how it could account for minioutbursts during quiescence. Moreover, a 1.96 hr period would produce a beat period of ∼3 days with the orbital period. Even taking into account the quasi-periodic nature of the minioutbursts, this period is longer than the typical interval between them, making it unlikely that the ∼1.96 hr period is associated with the minioutbursts.

While our power spectra do not show evidence of a superhump signal that could produce the minioutbursts by beating against the orbital period, the orbital modulation is so strong that it could potentially obscure the presence of a transitory, low-amplitude superhump signal. Thus, we cannot entirely rule out this possibility.

6. Conclusion

J0359 is the first eclipsing SU UMa-type system for which a superoutburst has been observed by *Kepler* in the short-cadence mode. There were eight normal, outside-in outbursts, one of which was a precursor to the superoutburst. Superhumps emerged near the maximum of the precursor and reached their maximum amplitude of ∼0.4 mag in just several orbits. The superhump amplitude fluctuated during the early-to-mid superoutburst and appeared to correlate with the orbital phase at which the superhump maximum occurred. This effect could be caused by orbital-phase-dependent obscuration of the superhump light source by an elevated, non-axisymmetric disk rim, or it could be related to the viewing aspect of the intrinsically asymmetric superhump light source as suggested by Osaki & Meyer (2003).

The mass ratio of J0359, estimated to be $q = 0.281 \pm 0.015$ from the period excess of Stage A superhumps, is marginally inconsistent with simulations of superhumps that predict a limiting mass ratio of $q = 0.25$ for superhump formation. However, the overlap between eclipses and half of the Stage A superhump maxima means that the uncertainty of our measurement might be underestimated, so an independent measurement of the mass ratio in a follow-up study would be very useful.

We detected a phase shift of the stream-disk hot spot toward earlier orbital phases after the superoutburst. We attribute the shift to a shrinkage of the disk radius after the superoutburst, as predicted by the TTI model.

J0359 also displayed a series of unusual minioutbursts that abruptly ceased after the superoutburst. Their cause remains elusive, and it would be beneficial if a future theoretical study were to attempt to incorporate them into the TTI model.

We thank the referee, Taichi Kato, for a comprehensive and expeditious report that significantly improved this paper.

P.S. acknowledges support from NSF grant AST-1514737 and is grateful for discussions of this object at the KITP Conference on Confronting MHD Theories of Accretion Disks with Observations.

Z.D. is supported by CAS Light of West China Program and the Science Foundation of Yunnan Province (No. 2016FB007). We thank Dr. Kai Li for observing J0359 at Weihai Observatory.

ORCID iDs

Colin Littlefield https://orcid.org/0000-0001-7746-5795
Peter Garnavich https://orcid.org/0000-0003-4069-2817
Mark Kennedy https://orcid.org/0000-0001-6894-6044
Paula Szkody https://orcid.org/0000-0003-4373-7777

References

Billington, I., Marsh, T. R., Horne, K., et al. 1996, MNRAS, 279, 1274
Cleveland, W. S. 1979, J. Am. Statist. Assoc., 74, 829
Drake, A. J., Djorgovski, S. G., Mahabal, A., et al. 2009, ApJ, 696, 870
Drake, A. J., Graham, M. J., Djorgovski, S. G., et al. 2014, ApJS, 213, 9
Howell, S. B., Sobeck, C., Haas, M., et al. 2014, PASP, 126, 398
Hu, S. M., Han, S. H., Guo, D. F., & Du, J. J. 2014, RAA, 14, 719
Kato, T., Dubovsky, P. A., Kudzej, I., et al. 2014, PASJ, 66, 90
Kato, T., Hambsch, F.-J., Dubovsky, P. A., et al. 2015, PASJ, 67, 105
Kato, T., Imada, A., Uemura, M., et al. 2009, PASJ, 61, S395
Kato, T., Ishioka, R., Isogai, K., et al. 2016, PASJ, 68, 107
Kato, T., Maehara, H., Miller, I., et al. 2012, PASJ, 64, 21
Kato, T., & Osaki, Y. 2013, PASJ, 65, 115
Kato, T., Pavlenko, E. P., Shchurova, A. V., et al. 2016, PASJ, 68, L4
Knigge, C., Baraffe, I., & Patterson, J. 2011, ApJS, 194, 28
Kotze, E. J., Potter, S. B., & McBride, V. A. 2015, A&A, 579, 77
Long, K. S., & Gilliland, R. L. 1999, ApJ, 511, 916
Lubow, S. H. 1991a, ApJ, 381, 259
Lubow, S. H. 1991b, ApJ, 381, 268
Murray, J. R. 1998, MNRAS, 297, 323
Murray, J. R., Warner, B., & Wickramasinghe, D. T. 2000, MNRAS, 315, 707
Orosz, J. A., & Hauschildt, P. H. 2000, A&A, 364, 265
Osaki, Y. 1974, PASJ, 26, 429
Osaki, Y. 1989, PASJ, 41, 1005
Osaki, Y., & Meyer, F. 2003, A&A, 401, 325
Osaki, Y., & Kato, T. 2013, PASJ, 65, 50
Osaki, Y., & Kato, T. 2014, PASJ, 66, 15
Ramsay, G., Wood, M. A., Cannizzo, J. K., Howell, S. B., & Smale, A. 2017, MNRAS, 469, 950
Shafter, A. W. 1983, ApJ, 267, 222
Smith, A. J., Haswell, C. A., Murray, J. R., Truss, M. R., & Foulkes, S. B. 2007, MNRAS, 378, 785
Stellingwerf, R. F. 1978, ApJ, 224, 953
Still, M., & Barclay, T. 2012, PyKE, Astrophysics Source Code Library ascl:1208.004
Webb, N. A., Naylor, T., Ioannou, Z., et al. 1999, MNRAS, 310, 407